COMPARISON OF THE PROPULSION PERFORMANCE OF AEROSPIKE AND BELL-SHAPED NOZZLE USING HYDROGEN PEROXIDE MONOPROPELLANT UNDER SEA-LEVEL CONDITION

A. Lai S. S. Wei C. H. Lai J. L. Chen Y. H. Liao J. S. Wu*

Department of Mechanics
National Chiao Tung University
Hsinchu, Taiwan

Y. S. Chen

Aerospace Engineering
TiSPACE Incorporated
Miaoli, Taiwan

ABSTRACT

This study investigates numerically the performance of applying aerospike nozzle in a hydrogen peroxide mono-propellant propulsion system. A set of governing equations, including continuity, momentum, energy and species conservation equations with extended k-ε turbulence equations, are solved using the finite-volume method. The hydrogen peroxide mono-propellant is assumed to be fully decomposed into water vapor and oxygen after flowing through a catalyst bed before entering the nozzle. The aerospike nozzle is expected to have high performance even in deep throttling cases due to its self-compensating characteristics in a wide range of ambient pressure environments. The results show that the thrust coefficient efficiency ($C_{f,\eta}$) of this work exceeds 90% of the theoretical value with a nozzle pressure ratio (*PR*) in the range of 20 ~ 45. Many complex gas dynamics phenomena in the aerospike nozzle are found and explained in the paper. In addition, performance of the aerospike nozzle is compared with that of the bell-shape nozzle.

Keywords: Hydrogen peroxide, Mono-propellant, Computational fluid dynamics, Aerospike nozzle.

1. INTRODUCTION

Rocket propulsion is one of the key technologies in various aerospace and space applications. A typical rocket propulsion system includes propellant tanks, flow control and plumbing system, combustion chamber and exhaust nozzle. In general, the performance of a propulsion system is described by *ISP* [1], which is the ratio of the obtained thrust and the mass flow rate. The higher this value, the more efficient this propulsion system is. Furthermore, the *ISP* is the product of two other parameters which are C^* and C_f, given in the equation $ISP \times g_0 = C^* \times C_f$. The C^* value is affected by the type of propellant used and the C_f value is dependent on the nozzle condition. A well designed nozzle can boost the thrust by further accelerating the gas after choking at the throat of the nozzle. Thus, how to optimize the design of exhaust nozzle is one of the critical tasks in designing a rocket propulsion system with high efficiency.

There are several different types of nozzle that one can find in the literatures for achieving the above purpose [1]. The most common one and most frequently used is known as the contour (bell-shaped) nozzle. This type of nozzle has an outer shell in a bell-like shape that guides the fluid to flow into the axial direction at the diverging (accelerating) part of the nozzle. This nozzle has been used in space society for decades. Some examples include V-2 rockets, Space Shuttle Main Engine, Saturn V and Falcon 9, to name a few. The benefit of this type of nozzle is that the working fluid flows inside the nozzle shell, which makes it relatively easy to design, fabricate and assemble. For long duration uses, regenerative cooling [2] is also feasible and easily implemented (with respect to the other designs). But due to the fixed shape and size (area ratio), each design of this type of nozzle has its optimal operating nozzle pressure ratio (*PR*) [3]. If the operating *PR* is lower than the designed *PR*, the flow is over expanded at the

* Corresponding author (chongsin@faculty.nctu.edu.tw)

DOI : 10.1017/jmech.2018.18

nozzle exit, which results in thrust lost and possible structural problem [4]; and if the operating *PR* is higher than the designed *PR*, the flow is under expanded at the nozzle exit, which also causes thrust lost. Both aforementioned cases result in thrust lost with a magnitude depending on the difference between the optimal and operating *PR*.

Another type of nozzle which has been seldom used in the rocket propulsion system is the aerospike (a.k.a. plugged) nozzle [5]. This type of nozzle has a spike at the center of the nozzle which guides the fluid to accelerate in the axial direction. The benefit of this type of nozzle is that the flow will expand to the ambient condition automatically. This leads to optimal expansion and produce maximal obtainable thrust in a wide range of ambient conditions. Some of the examples are the X-33 of Lockheed Martine, VentureStar, and some projects of Environmental Aeroscience Corporation (EAC). Yet there are several issues that a user must overcome in order to implement this type of nozzle. These include: 1) The hot gas encloses the "spike" during operation, which causes a challenging material problem since finding a material with such a small volume at the tip that can withstand the heat of the exhaust gas is very difficult; 2) The "spike" has to be held in place from the interior of the engine which can cause difficulty and coupling during design, and 3) For long duration operations, it is difficult to implement the regenerative cooling strategy often used in the bell-shaped nozzle.

Despite of the issues stated above, these challenges can be well waived by using mono-propellant hydrogen peroxide, even though its *ISP* is comparably low. It may find some specific application such as attitude control thruster of rocket and others such as levitating platform [6] using multiple thrusters without thrust vectoring control. For the material melting problem, the exhaust gas temperature of 1,023 K for using, e.g., 90% H_2O_2, is relatively low (compared with bi-propellant engines about 3,000 K) and metals such as steel can work well in this condition. The fixture used in holding the "spike" in place can be connected directly to the catalyst bed in the reacting zone of the engine which makes the implementation much easier. And finally, regenerative cooling is not required in this case since the temperature is not a critical issue at 1,023 K.

This work tries to design a mono-propellant aerospike engine using H_2O_2. A typical throttling method is by controlling the propellant injected to the engine. This will cause the chamber pressure to vary and so do the *PR*. Therefore, this work numerically investigates the propulsion performance of an aerospike nozzle for a 90% mono-propellant H_2O_2 engine under the effect of different *PRs* at sea level. Finally, a comparison of the bell-shaped and aerospike was conducted.

2. RESEARCH METHODS

This work first validates the current numerical tool by comparing with previous studies related to aerospike nozzle [7, 8]. Since the main focus of this article is the effect of the nozzle, other factors that may affect the performance are not included. For example, the reacting efficiency in the reacting zone of the engine is assumed to be perfect.

2.1 Numerical Method

The numerical tool used in this work is the all-speed UNIC-UNS code [9] that has a capability to solve a set of physical governing equations which include the mass conservation Eq. (1), momentum conservations Eq. (2), energy conservation Eq. (3) and species conservation Eq. (4) using pressure-based cell-centered finite volume method. To model the turbulence of the described flow field, the extended turbulence k-ε model Eq. (5, 6) [10] is used. For the equation of state, the HBMS (Hirschfelder, Beuler, McGee and Sutton) model Eq. (7, 8) [11] is used to describe the relationship between pressure, density and enthalpy. To analyze the nozzle flow fields, the problems are solved numerically using the time marching scheme. UNIC-UNS is a pressure-based multiphysics solver. Details of the numerical discretization and solution algorithm can be found in [9] and are not described here. Only the governing equations are summarized as follows for reference.

$$\frac{\partial \rho}{\partial t}+\frac{\partial}{\partial x_j}(\rho u_j)=0 \tag{1}$$

$$\frac{\partial}{\partial t}(\rho u_i)+\frac{\partial}{\partial x_j}(\rho u_i u_j)=\frac{\partial}{\partial x_j}\left(\mu\frac{\partial u}{\partial x_j}\right)-\frac{\partial P}{\partial x_i}+\rho g_i \tag{2}$$

$$\begin{aligned}\frac{\partial}{\partial t}(\rho h)+\frac{\partial}{\partial x_j}(\rho h u_j)&=\frac{\partial}{\partial x_j}\left[\left(\frac{K}{C_p}+\frac{\mu_t}{\sigma_h}\right)\left(\frac{\partial e}{\partial x_j}\right)\right]\\&+\frac{\partial}{\partial x_j}\left\{[(\mu+\mu_t)]\left(\frac{1}{2}\frac{\partial V^2}{\partial x_j}\right)\right\}\\&+\frac{\partial}{\partial x_j}\left[\left(\frac{K}{C_p}+\frac{\mu_t}{\sigma_h}\right)\left(\mu_k\frac{\partial u_j}{\partial x_k}-\frac{2}{3}u_j\frac{\partial u_k}{\partial x_k}\right)\right]\\&-\frac{\partial P}{\partial t}+Q_r\end{aligned} \tag{3}$$

$$\frac{\partial}{\partial t}(\rho\alpha_i)+\frac{\partial}{\partial x_j}(\rho\alpha_i u_j)=\frac{\partial}{\partial x_j}\left[\left(\rho D+\frac{\mu_t}{\sigma_\alpha}\right)\frac{\partial \alpha_i}{\partial x_j}\right]=\omega_i \tag{4}$$

$$\begin{aligned}\frac{\partial}{\partial t}(\rho k)+\frac{\partial}{\partial x_j}(\rho k u_j)&=\frac{\partial}{\partial x_j}\left[\left(u+\frac{\mu_t}{\sigma_k}\right)\frac{\partial k}{\partial x_j}\right]\\&+\rho(\Pi-\varepsilon)\end{aligned} \tag{5}$$

$$\begin{aligned}\frac{\partial}{\partial t}(\rho\varepsilon)+\frac{\partial}{\partial x_j}(\rho\varepsilon u_j)&=\frac{\partial}{\partial x_j}\left[\left(\mu+\frac{\mu_t}{\sigma_\varepsilon}\right)\frac{\partial \varepsilon}{\partial x_j}\right]\\&+\rho\frac{\varepsilon}{k}\left(C_1\Pi-C_2\varepsilon+C_3\frac{\Pi^2}{\varepsilon}\right)\end{aligned} \tag{6}$$

$$P_r=\sum_{j=1}^{4}T_r^{j-2}\sum_{i=1}^{6}B_{ij}\rho_r^{i-2} \tag{7}$$

$$\frac{H-H_0}{RT}=Z_c\int_0^{\rho_c}\left[\frac{P}{T_r}-\left(\frac{\partial P}{\partial T_c}\right)_{\rho_r}\right]\rho_r^{-2}d\rho_r+Z_c\frac{P}{\rho_r T_r}-1 \tag{8}$$

Table 1 Test conditions used in this study for case validation.

PR	P_c (bar)	P_a (bar)
6	6.0	1.0
15	15.0	1.0
340	34.0	0.1

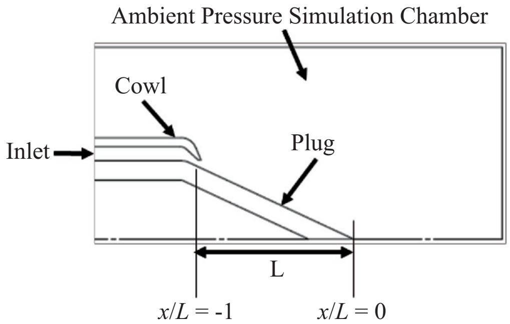

Fig. 1 Schematic diagram of the experimental setup Tomita *et al*. [7].

2.2 Code Validation for Aerospike Nozzle

To validate the code for the similar physical problems, we simulated the same *PRs* in the experimental and numerical studies of Tomita *et al*. [7] and Ito *et al*. [8] with the pressure values shown in Table 1, respectively. Figure 1 illustrates the sketch of the geometry of aerospike nozzle used by Tomita *et al*., which consists of a cowl, a cone-shaped plug that builds the nozzle system and an external chamber that can simulate the desired "ambient" or external pressure of the nozzle system. The working gas is compressed air. The respective numerical boundary settings are described in Table 2. This experiment investigated many cases including nozzle pressure ratios ($PR = P_c/P_a$) of 6, 15 and 340. Figure 2 shows the comparison of non-dimensional surface pressure, $(P\text{-}P_a)/P_c$, along the axial position x from the nozzle tip for different *PRs* between the present numerical study and Tomita *et al*.. Note x/L is a non-dimensional parameter defined as the ratio of axial position from the nozzle tip to the distance between nozzle tip and the throat. The results show that the pressure variations between the experiments and the current study are generally in reasonable agreement even though the deviations are larger for lower *PR*. For the case of *PR* 340, a smooth decaying curve similar to exponential line is observed due to pure supersonic expansion from the nozzle throat to the nozzle tip. For the case of *PR* 6 and 15, a negative value of $(P\text{-}P_a)/P_c$ is observed which indicates the presence of strong compression (or shock) waves along the surface. Normally, these waves will be accompanied by oblique shocks which is also observed in this work. The generation of shock waves is extremely dependent on the geometrical condition and will affect the pressure on the nozzle surface. Due to the reason that other than the major dimensions given in the reference, we made a reasonable guess on the non-stated dimensions. Therefore, the $(P\text{-}P_a)/P_c$ of the case with lower *PR* slightly deviates from those of Tomita *et al*. [7].

Table 2 Boundary conditions used in this study.

Boundary type	velocity	thermal
Inlet	Fixed total pressure to P_c	Room temperature
External (ambient)	Fixed total pressure to P_a	Fixed total temperature
Wall	No-slip	Adiabatic

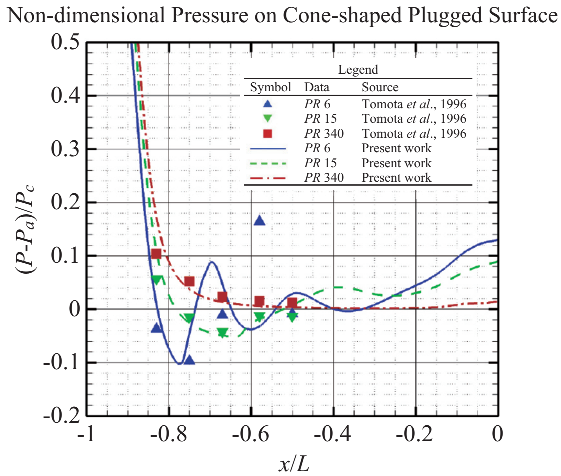

Fig. 2 Non-dimensional pressure along the nozzle surface as a function of non-dimensional distance from the tip for *PR* of 6, 15 and 340.

Figure 3 to Fig. 5 show the corresponding Mach number, pressure and temperature contours for *PR* of 6, 15 and 340, respectively. In the case of *PR* 6, we can see a train of compression and expansion waves (3 sets) that interacts throughout the exhaust flow above the nozzle surface causing the increasing and decreasing of Mach number, pressure and temperature values Figs. 3(a), (b) and (c). As the flow goes downstream, the intensity of the expansion and shock wave decreases, therefore the variation of these three also decreases. Similar phenomena is also observed in Fig. 4 for the case of *PR* 15 but the number of expansion and compression waves decreases to one since the *PR* is larger than the previous case. After the nozzle, a slightly stronger expansion is observed, then followed by a strong compression wave that initiates from x = -36 and causes the flow to detached from the plug surface. A negative $(P\text{-}P_a)/P_c$ is also observed at this point in Fig. 2 ($x/L \approx$ -0.7). This compression wave is accompanied by a decrease in Mach number observed in Fig. 4(a) and slight increase of temperature in Fig. 4(c). In Fig. 5 for the case of *PR* 340, a pure expansion is observed on the nozzle surface and the first shock initiates near the tip of the nozzle where the flow from the other half of the nozzle starts to interact with its counterpart. Due to the pressure compensation characteristic of the aerospike nozzle, the width of the exhaust

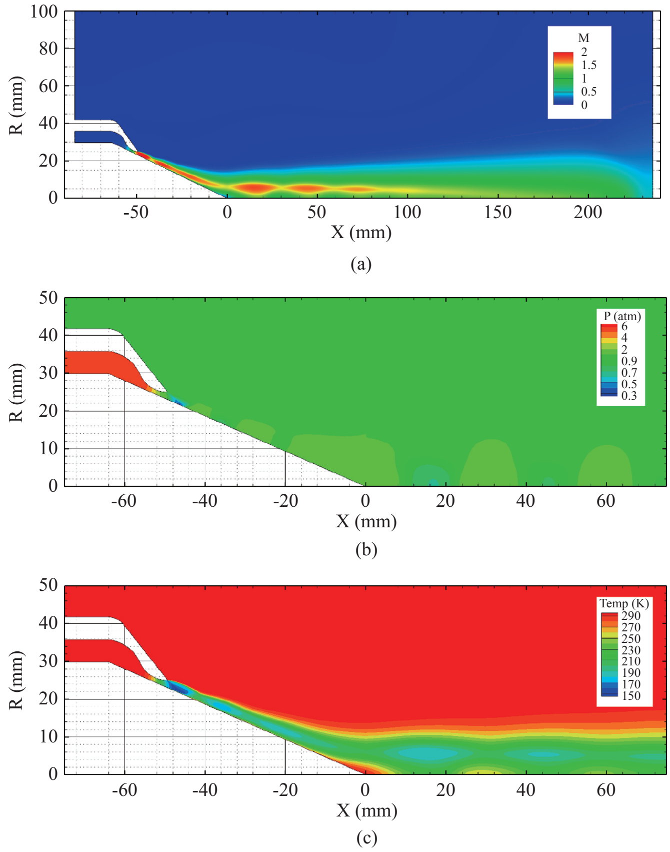

Fig. 3 (a) Mach number (b) pressure and (c) temperature contour of *PR* 6 for the case of Tomita *et al*. [7].

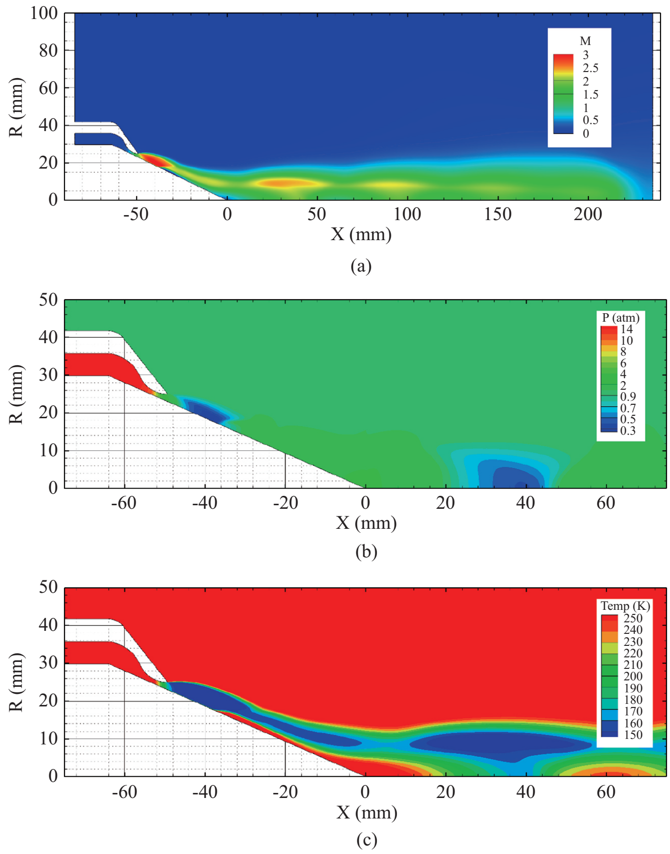

Fig. 4 (a) Mach number (b) pressure and (c) temperature contour of *PR* 15 for the case of Tomita *et al*. [7].

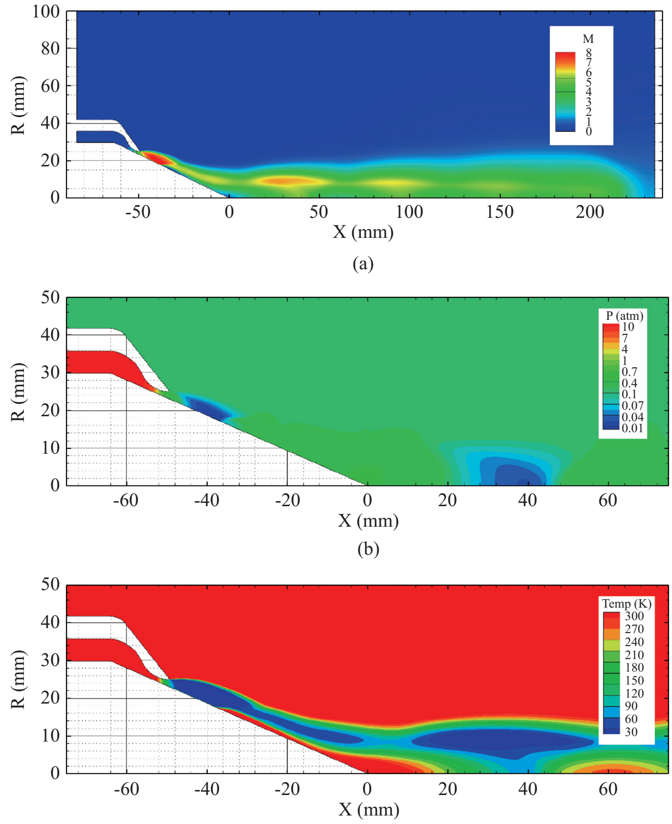

Fig. 5 (a) Mach number (b) pressure and (c) temperature contour of *PR* 340 for the case of Tomita *et al*. [7].

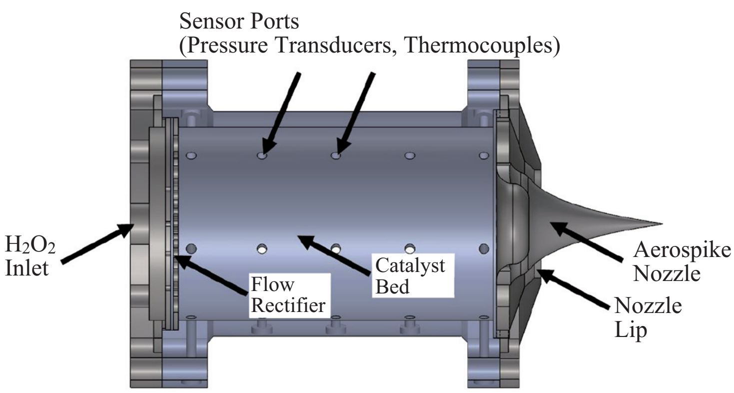

Fig. 6 Schematic diagram of H_2O_2 monopropellant engine.

plume increases as *PR* increases. All these Mach number patterns are the same as those of Ito *et al*. [8].

With the above comparisons with previous experimental and numerical studies of aerospike nozzle, we conclude that the numerical tool used in this work is sufficient to model the aerospike nozzle.

3. RESULTS AND DISCUSSION

This study proposes an aerospike nozzle that can be attached to an H_2O_2 catalyst bed for a monopropellant propulsion system application. A schematic diagram is shown in Fig. 6. This reactor is designed to operate at maximum chamber pressure (P_c) of 45 atm while the ambient pressure (P_a) of 1 atm (*PR* about 45). In this study, we would like understand the effect of various chamber pressures on the performance of the aerospike nozzle and compare with the conventional bell-shaped nozzle.

The computational domain is defined in the region behind the catalyst bed where almost all H_2O_2 has decomposed into H_2O and O_2 (assumed). The domain of interest is modeled using a 2-D axisymmetric method

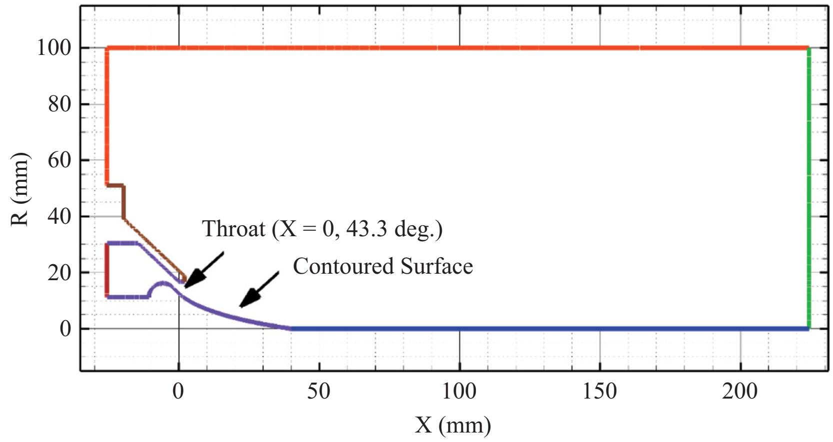

Fig. 7 Schematic diagram of the computational domain. Red line: inflow with fixed total pressure and temperature conditions, purple/brown line: wall with no-slip and adiabatic conditions, orange line: far-field condition, green line: supersonic outflow condition, blue line: axisymmetric axis.

Table 3 Parameters used in the designed aerospike nozzle.

Name	Dimension
Lip (cowl) diameter	33.54 (mm)
Lip (throat) width	2.93 (mm)
Inlet outer diameter	61.00 (mm)
Inlet inner diameter	22.50 (mm)
Throat angle	43.3 (deg.)
Lip (primary nozzle) length	2.00 (mm)
Throat area	289.10 (mm^2)
Primary nozzle area	504.76 (mm^2)
Initial nozzle ratio	~ 1.746
Overall nozzle ratio	~ 3.056
Far-field diameter	200 (mm)
Outlet distance from throat	225 (mm)

where the axis of rotation is the centerline of the propulsion system. A schematic diagram of the computational domain with rough dimension is shown in Fig. 7 with boundary conditions color coded and related detailed dimensions are summarized in Table 3. The inlet is indicated in red line, which is the interface of the catalyst bed and aerospike nozzle. At this boundary, a fixed total pressure and a total temperature were applied. The species flowing into the nozzle was defined as H_2O: O_2 = 0.5765: 0.4235 wt% (equivalent to 90% of $H_2O_{2(aq)}$ solution). The inlet total pressure ranged from 5 to 45 atm for the case study and the total temperature was 1,023 K, which is the adiabatic decomposition temperature of this solution. For the nozzle wall (purple lines), no-slip and adiabatic boundary conditions were applied. In this boundary, the simulated surface pressure applied to the wall was used to calculate the force and *ISP* of the propulsion system. The brown lines represent the outer-casing of the propulsion system for guiding the hot gas flow. At this boundary, no-slip and adiabatic boundary conditions were applied. Note that the pressure acting on this surface was the effect of external environment and would result in the drag force of the vehicle. This force was not considered in calculating the performance of the nozzle. The orange line indicates the far-field boundary condition, along which the total pressure is set to 1 atm. The green line is the supersonic flow outlet. The blue line is the axisymmetric centerline of the computational domain.

3.1 Grid Tests

To ensure that the resolution of the grid is sufficient, a series of grid test was performed. The case chosen for the grid test was the case with chamber pressure (P_c) of 30 atm. Four different mesh resolutions were used with cell numbers of 37 k, 62 k, 125 k and 192 k respectively. Figure 8 shows a typical time history of simulated mass flow rate, thrust and *ISP* history curve with a chamber pressure of 30 atm. The results show that a steady state of these parameters is reached after 0.002 s. Nevertheless, the external flow field (stream trace) is stable only after 0.006 s (though the performance of the nozzle is independent of the evolution of the external flow after a certain instant of time). Therefore, all these cases were

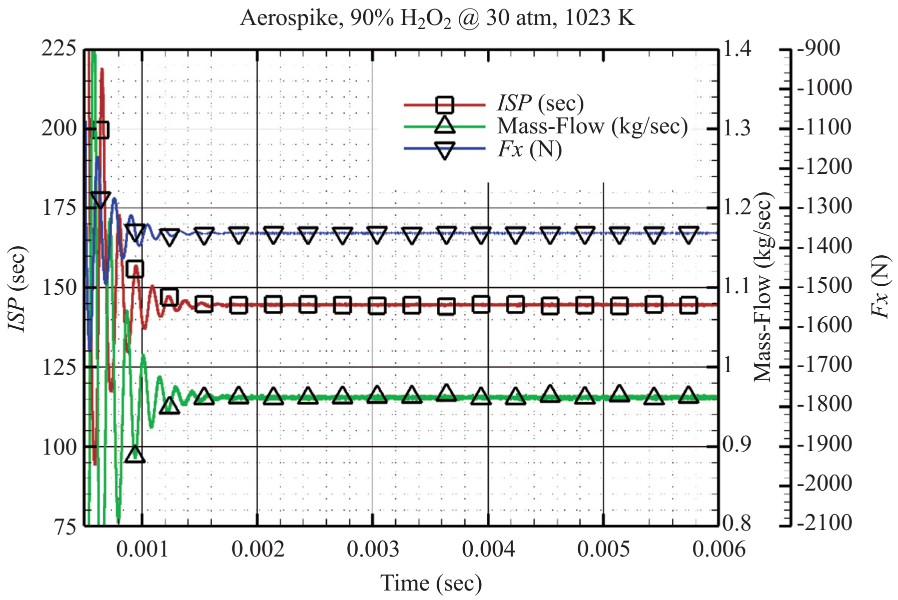

Fig. 8 Time history of thrust, mass flow rate and *ISP*.

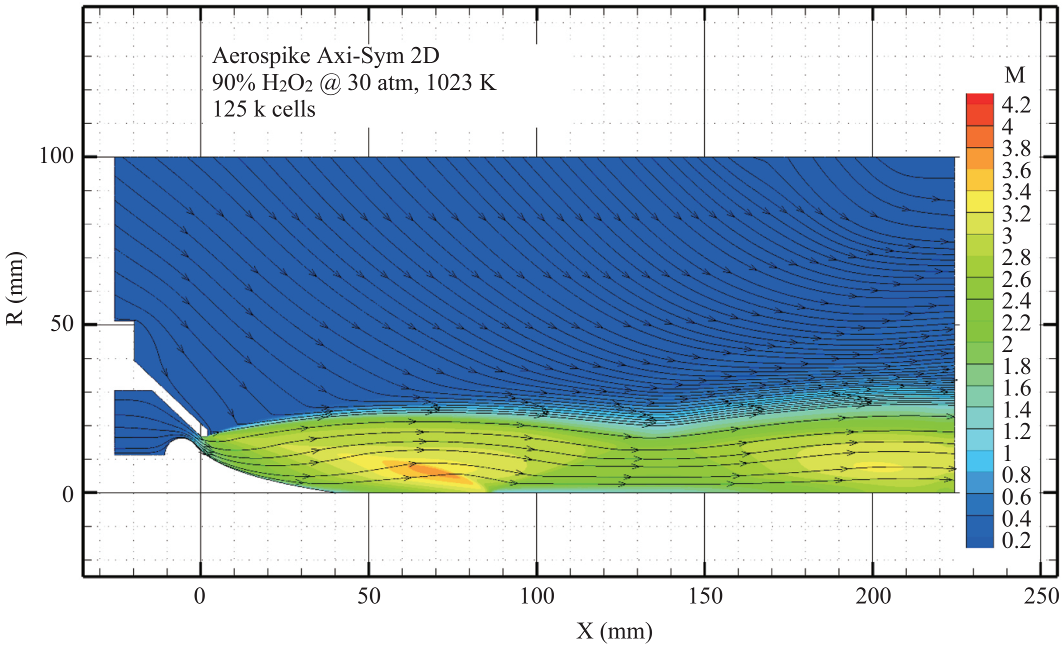

Fig. 9 Stream trace and Mach number contour of aerospike nozzle at 30 atm with 125 k cells. ($PR = 30$)

calculated up to the physical time of 0.006 s for comparison purpose. Figure 9 shows the stream trace with Mach number contour for the case of 125 k cells. We can observe that there is a clear barrier between the ambient air and the exhaust flow. A strong entrainment of the ambient air is also observed near this barrier. The pressure contour is shown in Fig. 10. In this case, the flow experience a smooth expansion from the throat to the tip of the plug. To make sure that the resolution is enough, some calculated properties are summarized in Table 4. The error of mass flow rate ($\dot{m}$), relative to the case of 192 k cells, has a maximum value of 1.37% in the case of 37 k cells and less than 1% for the cases of 62 k and 125 k cells. For the integrated propulsive force (F), the maximum error occurs in the case of 62 k cells with the value of 0.59%. In these four cases, the maximum error of ISP_{vac} is found for the case of 37 k cells with a value of -1.23%.

In addition to the grid test, we also tested whether the downstream "far field" distance is sufficiently far enough so that it will not affect the computational results. In this study, we used a grid resolution similar to the case of 125 k, but extended the "x" boundary 1.5 times and "R" boundary 2.0 times the original setup. Figure 11 and Fig. 12 shows the results of Mach number and Pressure contour using 177 k cells are essentially the same as

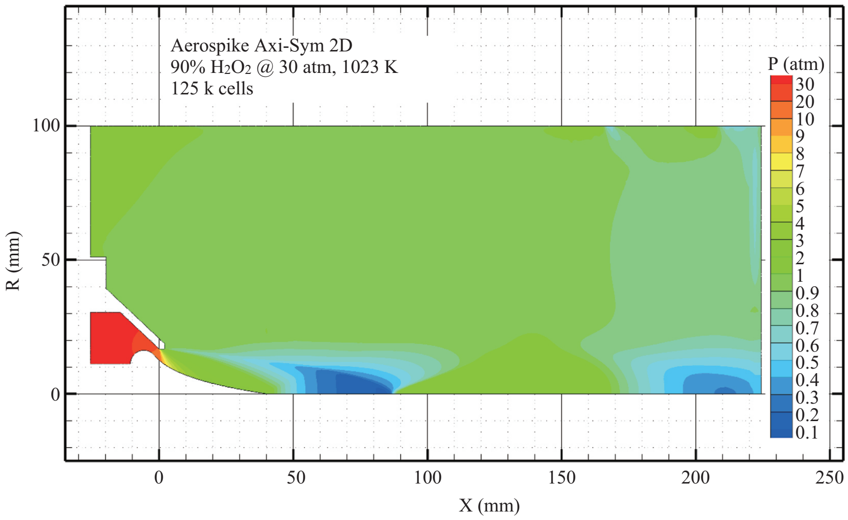

Fig. 10 Pressure contour of aerospike nozzle at 30 atm with 125 k cells. (PR = 30)

Table 4 Grid test result of aerospike nozzle case of 30 atm chamber pressure. (PR = 30)

Case		37 k	62 k	125 k	177 k	192 k
* Mass Flow (kg/s)	$\dot{m}$	0.97	0.96	0.96	0.96	0.95
C^* (m/s)	$= (P_c^* A_t)/\dot{m}$	919.31	922.99	924.56	924.64	931.94
(error, %)		1.37	0.97	0.80	0.79	-------
* Force (N)	F	1359.72	1365.92	1362.82	1362.78	1357.96
$C_{f,vac}$ (-)	$= F/(P_c^* A_t)$	1.53	1.54	1.53	1.53	1.53
(error, %)		0.13	0.59	0.36	0.35	-------
ISP_{vac} (s)	$= F/\dot{m}$	143.45	144.68	144.60	144.60	145.23
(error, %)		-1.23	-0.38	-0.44	-0.43	-------
				* time averaged value from t = 0.004 to 0.006 error = (value (192 k) – value (case))/value(192 k) × 100%		

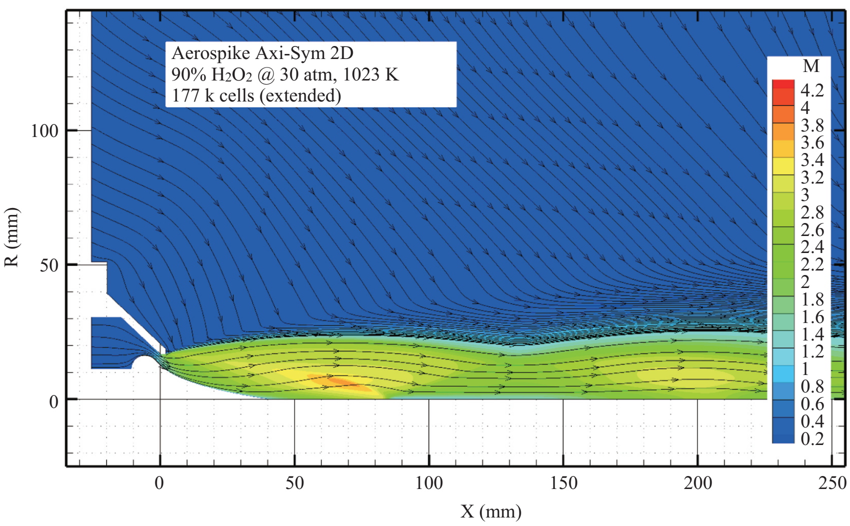

Fig. 11 Stream trace and Mach number contour of aerospike nozzle at 30 atm with 177 k cells. (PR = 30)

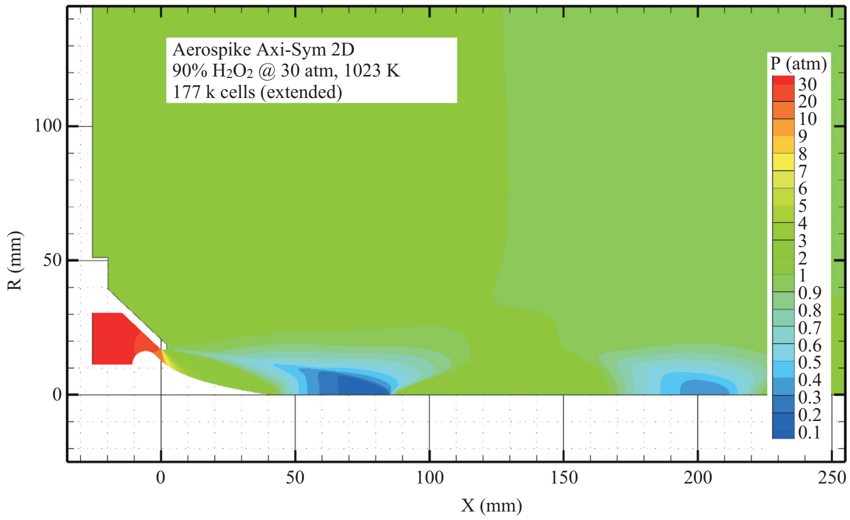

Fig. 12 Pressure contour of aerospike nozzle at 30 atm with 177 k cells. (PR = 30)

Table 5 Results of aerospike nozzle at various operating chamber pressures.

Case	5 atm	15 atm	20 atm	25 atm	30 atm	35 atm	40 atm	45 atm
PR (-)	5	15	20	25	30	35	40	45
* $\dot{m}$ (kg/s)	0.16	0.48	0.64	0.80	0.96	1.12	1.28	1.44
* F (N)	244.43	679.46	907.06	1134.92	1362.82	1590.72	1818.65	2046.59
ISP_{vac} (s)	157.17	144.56	144.56	144.58	144.45	144.61	144.63	144.64
ISP_{ground} (s)	99.59	125.41	130.18	133.06	134.97	136.35	137.38	138.18
ISP_η	0.63	0.87	0.90	0.92	0.93	0.94	0.95	0.96
C^* (m/s)	933.89	926.99	925.83	925.11	924.56	924.25	923.97	923.76
$C_{f,vac}$ (-)	1.65	1.53	1.53	1.53	1.53	1.53	1.53	1.53
$C_{f,ground}$ (-)	1.06	1.34	1.40	1.43	1.45	1.46	1.48	1.49

* time averaged value from t = 0.004 to 0.006

those of Fig. 9 and Fig. 10. Corresponding derived propulsion properties in this case are also included in Table 4. Based on the above numerical experiments, we have decided to use 125 k cells for the all the cases presented next unless otherwise specified, considering the computational time and accuracy of the simulation.

3.2 Aerospike Nozzle Case Study

Next, we try to investigate the effect of throttling on the propulsion performance. For this study, different chamber pressures (P_c) were used to simulate level of throttling. The pressures used are 5, 15, 20, 25, 30, 35, 40 and 45 atm. The Mach number and pressure contour of PR 15 to 45 are very similar to Fig. 9 and Fig. 10. The calculated propulsion related properties are summarized in Table 5. Due to the choking condition at the throat of the nozzle, the mass flow rate and corresponding integrated thrust are both proportional to the chamber pressure as expected. The ISP_{vac} was found to be nearly constant with a value of ~144.5 s, except for an extremely high value for the case of 5 atm, which will be explained later. The ground ISP (ISP_{ground}) was also evaluated by subtracting the back pressure from the integrated force as $ISP_{ground} = (F - P_a^* A_e)/\dot{m}$, where A_e is the nozzle exit area. Since the back pressure is 1 atm in the current study, the ISP_{ground} decreases with decreasing chamber pressure. The ISP_{ground} and the corresponding ISP efficiency ($ISP_\eta = ISP_{ground}/ISP_{vac}$) of the studied aerospike nozzle ranges from 100 to 138 s and from 63% to 96%, respectively. Thrust coefficient ($C_{f,vac}$) is defined by the ratio of overall force obtained by the nozzle (F) and the pressure force at the throat ($P_c^* A_t$). Under vacuum condition, $C_{f,vac}$ is only a function of the nozzle configuration. In this study, the aerospike nozzle shape was fixed; therefore, the $C_{f,vac}$ is a constant value 1.53. But for $C_{f,ground}$, the effect of the back pressure shall be deducted. Therefore, $C_{f,ground}$ is also a function of chamber pressure. In these cases, the minimum value is 1.06 at 5 atm and maximum value is 1.49 at 45 atm. The Mach number and pressure contours of PR 5 are shown in Fig. 13 and Fig. 14 respectively. In this case,

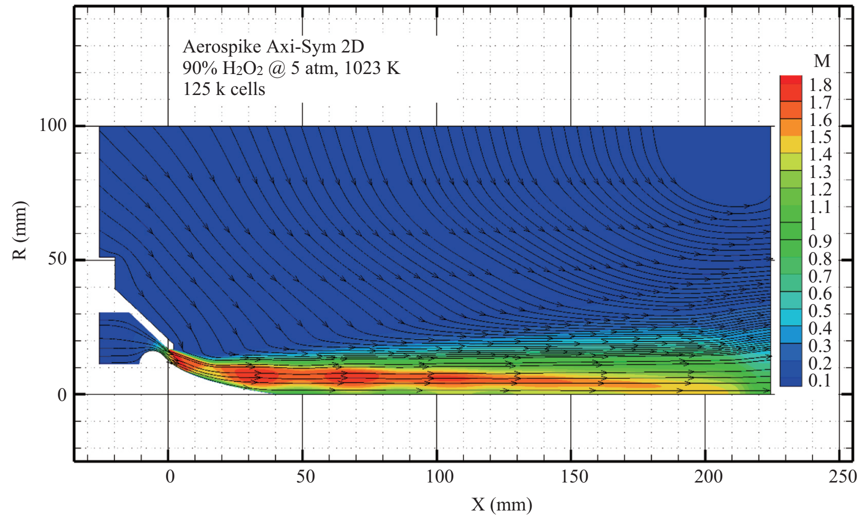

Fig. 13 Stream trace and Mach number contour of aerospike nozzle at 5 atm with 125 k cells. ($PR = 5$)

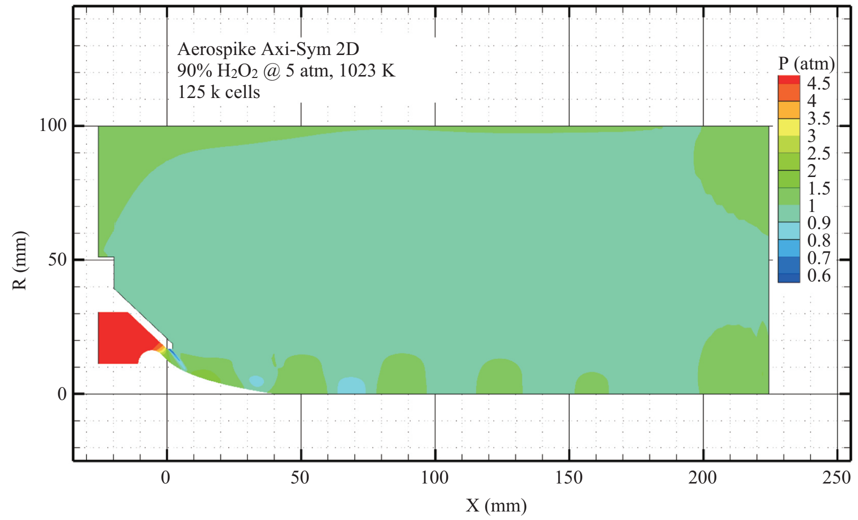

Fig. 14 Pressure contour of aerospike nozzle at 5 atm with 125 k cells. ($PR = 5$)

the PR is too low that compression and oblique shocks occurs at the plug surface. Therefore, the ISP_{vac} is relatively higher than those of the other cases.

3.3 Bell-Shaped Nozzle Case Study

To investigate the difference between aerospike and bell-shaped nozzles, we conducted a similar setup with contoured bell-shaped nozzle. Table 6 summarizes the dimensions used in designing the bell-shaped nozzle. The bell-shaped nozzle cases also underwent a series of grid test and the errors of the results were analyzed. The simulations were set to run for 0.006 s. Since the bell-shaped nozzle has a fixed expansion ratio. The ratio used in this study is chosen to be 4, which is the case of inviscid supersonic expansion when the chamber pressure is 30 atm. To summarize, there are three cases with different grid densities and one extended computational domain, namely 39 k, 126 k, 196 k and 174 k

Table 6 Parameters used in the designed bell-shaped nozzle.

Name	Dimension
Throat diameter	19 (mm)
Exit diameter	38 (mm)
Inlet diameter	28.35 (mm)
Throat area	283.53 (mm^2)
Exit area	1134.11 (mm^2)
Nozzle (expansion) ratio	4
Far-field diameter	200 (mm)
Outlet distance from throat	200 (mm)

(extended) respectively, which are similar to those of aerospike case study. Table 7 summarizes the result of mass flow rate ($\dot{m}$), thrust (F), ISP_{vac}, C^* and $C_{f,vac}$. The

Table 7 Grid test result of bell-shaped nozzle case at 30 atm. (PR = 30)

Case		39 k	126 k	174 k	196 k
* Mass Flow (kg/s)	$\dot{m}$	0.92	0.92	0.92	0.92
C^* (m/s)	$= (P_c^* A_t)/\dot{m}$	934.40	935.02	935.02	935.03
(error, %)		0.066	0.0007	0.0003	-------
* Force (N)	F	1260.78	1261.13	1261.18	1261.71
$C_{f,vac}$ (-)	$= F/(P_c^* A_t)$	1.46	1.46	1.46	1.46
(error, %)		-0.073	-0.046	-0.042	-------
ISP_{vac} (s)	$= F/\dot{m}$	139.52	139.64	139.65	139.71
(error, %)		-0.14	-0.046	-0.042	-------
		* time averaged value from t = 0.004 to 0.006 error = (value (196 k) – value (case))/value(196 k) × 100%			

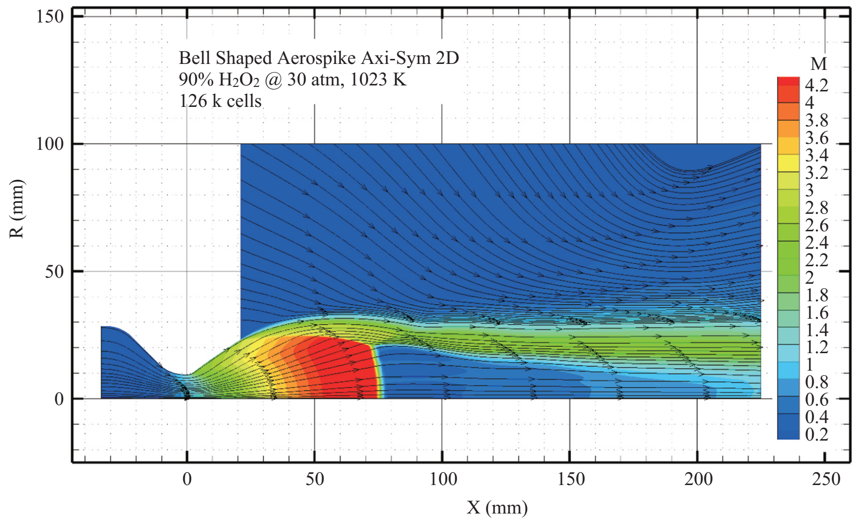

Fig. 15 Stream trace and Mach number contour of bell-shaped nozzle at 30 atm with 126 k cells. (PR = 30)

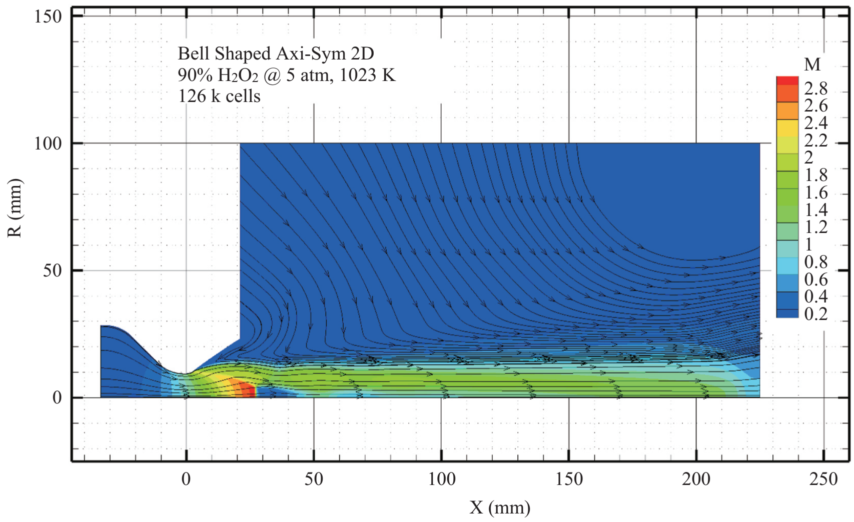

Fig. 16 Stream trace and Mach number contour of bell-shaped nozzle at 5 atm with 126 k cells. (PR = 5)

errors of these cases are all less than 0.15% which is essentially no difference. To minimize controversy for comparison, the case chosen for further study is 126 k cells one.

After the grid test, various chamber pressure conditions, similar to those of aerospike, were investigated. Figure 15 shows the stream traces and Mach number contour for the case of 30 atm chamber pressure. Pure expansion was observed in the divergent part of the nozzle and a clear Mach disk appeared at x = 75. As expected, both the mass flow rate and thrust are proportional to the chamber pressure except for the case of 5 atm. For the case of 5 atm, the expansion ratio of 4 which is too large for this low PR case. Corresponding results of stream traces and Mach number contour is shown in Fig. 16, in which a large amount of external air

Table 8 Results of bell-shaped nozzle at various operating chamber pressures.

Case	5 atm	15 atm	20 atm	25 atm	30 atm	35 atm	40 atm	45 atm
PR (-)	5	15	20	25	30	35	40	45
* $\dot{m}$ (kg/s)	0.15	0.46	0.61	0.77	0.92	1.08	1.23	1.38
* F (N)	314.26	634.81	841.39	1050.80	1261.13	1471.61	1682.12	1892.61
ISP_{vac} (s)	209.79	140.65	139.71	139.53	139.50	139.50	139.50	139.50
ISP_{ground} (s)	125.91	112.81	118.85	122.84	125.60	127.59	129.08	130.24
ISP_η	0.60	0.80	0.85	0.88	0.90	0.91	0.92	0.93
C^* (m/s)	940.47	936.39	935.72	935.30	935.02	934.81	934.66	934.53
$C_{f,vac}$ (-)	2.19	1.47	1.46	1.46	1.46	1.46	1.46	1.46
$C_{f,ground}$ (-)	1.31	1.18	1.25	1.29	1.32	1.34	1.35	1.37

* time averaged value from t = 0.004 to 0.006

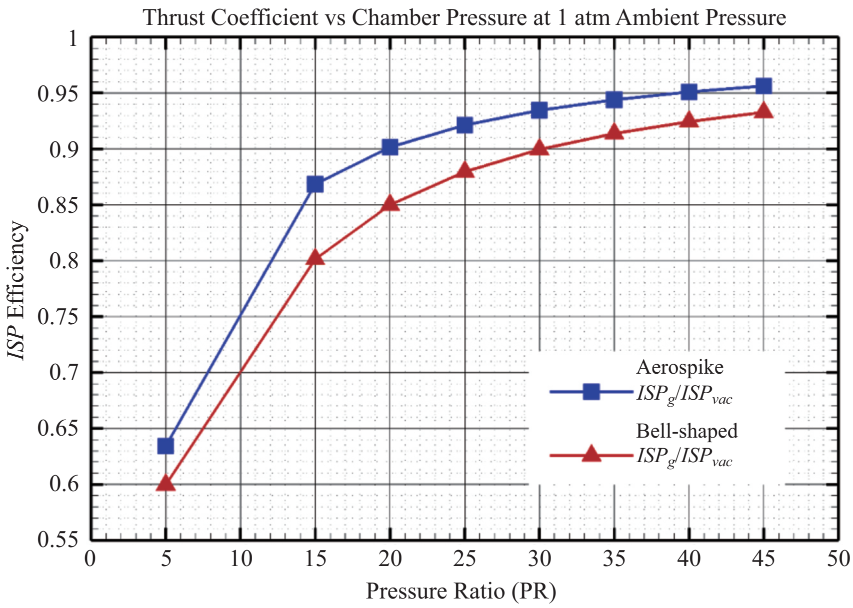

Fig. 17 Comparison of ISP_η of aerospike and bell-shaped nozzles with varying PRs.

is entrained into the inner divergent part of nozzle. This causes a pressure rise of the nozzle inner wall and leads to undesired resonance [12, 13]. This phenomenon is very critical to nozzle and may cause the permanent damage of the nozzle structure. Therefore, it is generally difficult for most propulsion systems to perform very deep throttling under this kind of condition. The ISP_{vac} and ISP_{ground} was also calculated using the method described in the aerospike cases. The ISP_{vac} remains at a constant value of 140 s while the ISP_{ground} increases with increasing of P_c. The ISP_η increases from 80% to 93% as P_c goes from 15 to 45 atm. Similar to the ISP, $C_{f,vac}$ of the fixed nozzle is a constant of 1.46 while $C_{f,ground}$ ranges from 1.18 to 1.37.

Since both cases have similar operating conditions, we plotted the results of ISP_η (Table 5 and Table 8) in Fig. 17 under varying pressure ratio (PR) for comparing the propulsion performance. The results clearly show that aerospike nozzle performs better than bell-shaped nozzle in a wide range of pressure ratios in the current study.

4. CONCLUSIONS

Two types of nozzles are being investigated numerically in this work, namely aerospike and conventional bell-shaped. To validate the numerical tool used, we benchmarked our simulations with previous studies [7, 8] with reasonable agreement. A series of investigation is performed to test the effect of various pressure ratios under sea level environment. The back pressure effect was subtracted to observe the sea level performance of these nozzles. The ISP_η (or $C_{f,\eta}$) increases as the chamber pressure (P_c) increases and the performance of the aerospike nozzle surpass those of bell-shaped ones. Furthermore, at very low PR, the aerospike nozzle is still operable while the bell-shaped counterpart is not. Therefore, we conclude that the aerospike nozzle is suitable for a propulsion system that requires very deep throttling capabilities near sea level condition.

ACKNOWLEDGEMENTS

This work was supported by Advanced Rocket Research Center (ARRC), National Chiao Tung University of Taiwan, and Ministry of Science and Technology (MOST) of Taiwan through a grant No. 105-2221-E-009-066-MY2.

NOMENCLATURES

B_{ij}	[-]	polynomial coefficients of thermophysical properties
C_1, C_2, C_3	[-]	modeling constants in the turbulence dissipation rate equation
C_p	[J/K]	isobaric specific heat
D	[m^2/s]	molecular diffusivity
H	[J/kg] or [m^2/s^2]	real-fluid total enthalpy
H_0	[J/kg] or [m^2/s^2]	ideal-gas total enthalpy
K	[W/m-K]	thermal conductivity
k	[J/kg] or [m^2/s^2]	turbulent kinetic energy
P	[N/m^2]	pressure
P_c	[N/m^2]	critical pressure
T	[K]	temperature
T_c	[K]	critical temperature
T_r	[-]	reduced temperature, $T_r = T/T_c$
t	[s]	time
u_i, u_j, u_k	[m/s]	velocity component in i, j, k direction
V	[m/s]	velocity magnitude
x	[m]	spatial coordinate
Z_c	[-]	compressibility factor at the critical condition
α_i, α_j	[-]	mass fraction of species i, j
ε	[J/kg-s] or [m^2/s^3]	turbulence dissipation rate
μ	[N-s/m^2]	dynamic viscosity
μ_t	[N-s/m^2]	turbulent eddy viscosity
Π	[J/kg-s] or [m^2/s^3]	production rate of turbulent kinetic energy
ρ	[kg/m^3]	fluid density
ρ_c	[kg/m^3]	critical density
ρ_r	[-]	reduced density, $\rho_r = \rho/\rho_c$
σ_H	[-]	Schmidt number for the energy equation
σ_k	[-]	Schmidt number for the turbulent kinetic energy equation
σ_α	[-]	Schmidt number for the species conservation equation
σ_ε	[-]	Schmidt number for the turbulence dissipation rate equation
$\partial/\partial t$	[1/s]	time derivative of the variable of interest
$\partial/\partial x$	[1/m]	spatial derivative of the variable of interest in the i, j, k direction

REFERENCES

1. Sutton, G. P. and Biblarz, O., *Rocket Propulsion Elements*, 7th Edition, JOHN WILEY & SONS INC., City of Publication (2001).
2. Marchi, C. H., Laroca, F., de Silva, A. F. C. and Hinckel, J. N., "Numerical Solutions of Flow in Rocket Engines with Regenerative Cooling," *Numerical Heat Transfer, Part A: Applications*, **45**, pp. 699-717 (2004).
3. Frey, M. and Hagemann, G., "Restricted Shock Separation in Rocket Nozzles," *Journal of Propulsion and Power*, **16**, pp. 478-484 (2000).
4. Loh, C. Y. and Zaman, K. B. M. Q., "Numerical Investigation of Transonic Resonance with a Convergent–Divergent Nozzle," *AIAA Journal*, Doi.org/10.2514/2.1607
5. Wasko, R. A., "Performance of Annular Plug and Expansion-Deflection Noozles Including External Flow Effects at Transonic Mach Numbers," *NASA Technical Note*, NASA TN D-4462 (1968).
6. Liu, Y.L. *et al*., "Development of a Quad Hybrid Rocket Engine Levitating Platform," *2nd International Conference on Aerospace Engineering (ICOAE 2018),* Seoul, Korea (2018).
7. Tomita, T., Tamura, H. and Takahashi, M., "An Experimental Evaluation of Plug Nozzle Flow Field," *AIAA, ASME, SAE, and ASEE, Joint Propulsion Conference and Exhibit*, Florida, U.S.A (1996).
8. Ito, T., Fujii, K. and Hayashi, A. K., "Computations of Axisymmetric Plug-Nozzle Flowfelds: Flow Structures and Thrust Performance," *Journal of Propulsion and Power*, **18**, pp. 254-260 (2002).
9. Chen, Y. S. *et al*., "Multiphysics Simulations of Rocket Engine Combustion," Computers & Fluids, **45**, pp. 29-36 (2011).
10. Chen, Y. S. and Kim, S. W., "Computation of Tur-

bulent Flows Using an Extended k-epsilon Turbulence Closure Model," *NASA Contractor Report*, NASA CR-179204, NASA-Marshall Space Flight Center Marshall Space Flight Center, Alabama (1987).

11. Cheng, G. C. and Farmer, R., "Real Fluid Modeling of Multiphase Flows in Liquid Rocket Engine Combustors," *Journal of Propulsion and Power*, **22**, pp. 1373-1381 (2006).
12. Lárusson, R., Andersson, N., Eriksson, L.-E. and Östlund, J., "Investigation of a Separated Nozzle Flow with Transonic Resonance Using Dynamic Mode Decomposition," *Chalmers Research Report*, ISSN, pp. 1652-8549 (2014).
13. Dippold III, V. F. and Zaman, K. B. M. Q., "An Investigation of Transonic Resonance in A Mach 2.2 Round Convergent-Divergent Nozzle," *AIAA 2015 SciTech* (2015).

(Manuscript received November 9, 2017,
accepted for publication March 12, 2018.)